

Investigation on Structural and Optical Properties of Sodium ion (Na^+) Doped Layered Perovskite Sr_2CeO_4

Dharmendra Yadav (✉ dharmendrayadav3991@gmail.com)

Indian Institute of Technology BHU Varanasi

Gurudeo Nirala

Indian Institute of Technology BHU Varanasi

Upendra Kumar

Banasthali Vidyapith

Shail Upadhyay

Indian Institute of Technology BHU Varanasi

Research Article

Keywords: Sr_2CeO_4 , XRD, Raman Spectrum, Oxygen vacancies, Photoluminescence

Posted Date: August 3rd, 2020

DOI: <https://doi.org/10.21203/rs.3.rs-50721/v1>

License:  This work is licensed under a Creative Commons Attribution 4.0 International License.

[Read Full License](#)

Investigation on structural and optical properties of sodium ion (Na⁺) doped layered perovskite Sr₂CeO₄

Dharmendra Yadav ^a, Gurudeo Nirala ^a, Upendra Kumar ^b and Shail Upadhyay ^a *

^aDepartment of Physics, Indian Institute of Technology (BHU) Varanasi, Uttar Pradesh-221005, India.

^bDepartment of Physics, Banasthali Vidyapeeth, Banasthali, Jaipur, Rajasthan- 304022, India.

Corresponding Author: Email: supadhyay.app@itbhu.ac.in

Abstract

Powder and ceramic of a few compositions of system Sr₂Ce_{1-x}Na_xO₄ (x=0, 0.02, 0.04, 0.06 and 0.10) were prepared by the conventional solid-state reaction method. The phase and structure of the synthesized samples were investigated by x-ray diffraction technique. The analysis of XRD data indicated that in Sr₂CeO₄, substitution sites of Na¹⁺ ions depend on the doping concentration. Na¹⁺ ions occupy Ce-sites when concentration is x = 0.02. With increasing doping amount (x=0.04, 0.06 and 0.10) Na¹⁺ substituted into both Sr and Ce site. Purity of the synthesized samples was reconfirmed using Raman and Fourier Transformation Infrared (FTIR) spectroscopy techniques. The optical band gap was recorded by UV-Vis absorption spectra; optical band gap energy of the samples lies between 2.91 - 3.10 eV. Room temperature photoluminescence (PL) measurements show that there two excitation peaks located around 290 nm and 350 nm. For Na doped samples, intensity of higher wavelength peak is more than the lower wavelength peak making them suitable candidate for UV excitation source. All the Na¹⁺ doped samples display an intense blue emission at 472 nm similar to undoped Sr₂CeO₄. But the intensity of emission for the doped samples is weak as compared to undoped sample. Scanning electron microscopic studies of fractured surfaces of the sintered pellets have indicated that dopant Na has played a significant role in the grain growth. Grain size and morphology of Na doped samples are different from undoped Sr₂CeO₄.

Keywords: Sr₂CeO₄; XRD; Raman Spectrum; Oxygen vacancies; Photoluminescence.

1 Introduction

On account of the high thermal and chemical stability, the oxide-based phosphors have attracted interest of researchers. These oxides phosphors are widely used for light emitting diodes, field emitters, plasma display panels and scintillator panels for X-ray radiography [1,2]. The oxide phosphors with blue light emission have significant importance because blue color light can be mixed with green, orange, and red color light in a definite ratio to get other colors. It is reported that Eu^{3+} doped $\text{BaMgAl}_{10}\text{O}_{17}$ oxide emits blue light but needs high calcination temperature (1400 -1600 °C) and reduce atmosphere to change the valence state of lanthanide Eu from Eu^{3+} to Eu^{2+} [3]. For the first time Danielson and his group synthesized another blue light emitting phosphor material (Sr_2CeO_4) by combinatorial route [4]. Thereafter, this phosphor drawn attention of the researchers due to its special structure and excellent luminescence performance. The structure of Sr_2CeO_4 is orthorhombic and space group Pbam. Sr_2CeO_4 structure consists of unusual one-dimensional chains of edge-shared CeO_6 octahedral along [001] [5]. Broad emission spectrum of Sr_2CeO_4 makes this oxide material a promising matrix for various activators [6–8]. Photoluminescence properties of this oxide has been investigated widely [9–16]. Doping of rare earth ions (Eu^{3+} , Ho^{3+} , Er^{3+} , Tm^{3+} , Sm^{3+} , Dy^{3+} , Nd^{3+}) at Sr^{2+} has been made to improve the photo luminescent properties of Sr_2CeO_4 [17–24]. In the last two decades researchers have paid attention mainly to photoluminescence of properties of Sr_2CeO_4 . But now researchers are diverting their attention towards other physical properties of this oxide which is require to make this material multifunctional. Recently dielectric properties have been investigated to use it for microwave dielectric application [25]. High temperature electrical conductivity and dielectric relaxation phenomenon of this material have been studied [26]. Protonic conductivity of $\text{Sr}_2\text{Ce}_{0.95}\text{Yb}_{0.05}\text{O}_4$ sample has been measured as a function of temperature (300–900°C), and (40–2500 Pa) to explore its application as proton conducting electrolyte in SOFCs [27]. Recently surfactant free synthesis of nanostructure Sr_2CeO_4 has been carried for its application in removal of organic pollutions [28].

An extensive literature survey has indicated that studies on tuning optical properties of Sr_2CeO_4 by substituting ions at Ce^{4+} sites are limited. To the best of our knowledge only Yb^{3+} , Er^{3+} , Nd^{3+} and Sn^{4+} ions have been substituted at Ce^{4+} sites of Sr_2CeO_4 [23,29–31]. No report on the effect of Na^{1+} ions doping at Ce^{4+} ions on the structure and properties of Sr_2CeO_4 has been

found in the literature. Though, the effect of co-doping alkali ions (Li^+ , Na^+ and K^+) with RE^{3+} ions at Sr^{2+} sites on luminescence properties of Sr_2CeO_4 have been studied [32–34]. Therefore, in this work a few compositions of the system $\text{Sr}_2\text{Ce}_{1-x}\text{Na}_x\text{O}_{4-\delta}$ (with $x = 0.00, 0.02, 0.04, 0.06$ and 0.10) have been synthesized by solid state reaction method. In this work, the substitution of Na^{1+} at Ce^{4+} was aimed to achieve improvement in the photoluminescence properties and electrical conductivity by increasing the number of oxygen vacancies. A systematic study on structural, optical properties and microstructure has been performed in detail for the possible applications of the synthesized materials.

2 Experimental Section

2.1 Synthesis Process

Powder of a few compositions of $\text{Sr}_2\text{Ce}_{1-x}\text{Na}_x\text{O}_4$ (with $x = 0.00, 0.02, 0.04, 0.06$ and 0.10) has been synthesized by solid state reaction method. In the text and figures the synthesized compositions of the system $\text{Sr}_2\text{Ce}_{1-x}\text{Na}_x\text{O}_4$ with $x = 0.00, 0.02, 0.04, 0.06$ and 0.01 , has been referred by abbreviated name S2CN0, S2CN2, S2CN4, S2CN6 and S2CN10, respectively. The abbreviated name S2CN0 refers to sample Sr_2CeO_4 and S2CN2 to sample $\text{Sr}_2\text{Ce}_{0.98}\text{Na}_{0.02}\text{O}_4$ and so on.

In this work raw materials SrCO_3 (Alfa Aesar, Purity 99.9%), Cerium oxide CeO_2 and $\text{Na}_2\text{CO}_3 \cdot \text{H}_2\text{O}$ (Alfa Aesar, Purity 99.9%) were used to synthesize the samples. CeO_2 was obtained from the heat treatment of ammonium nitrate $(\text{NH}_4)_2\text{Ce}(\text{NO}_3)_6$ (Alfa Aesar, Purity 99.5%) at 500°C . For the estimation of percentage of CeO_2 in $(\text{NH}_4)_2\text{Ce}(\text{NO}_3)_6$ was taken into a small alumina crucible and thermogravimetric (TG) analysis carried out. Thermal analysis data of $(\text{NH}_4)_2\text{Ce}(\text{NO}_3)_6$ was in this work is shown in our earlier work on Na^+ doped SrCeO_3 system. The stoichiometric amount of raw materials in presence of acetone (as mixing media) were milled in a planetary ball-mill (PM200, Retsch, Germany) using zirconia balls for 8 h at 200 rpm. The ball-milled powders were later dried in an oven for 12 h. Thermal analysis (TG and DSC) of a stoichiometric mixture of raw materials for sample S2CN4 was carried out using simultaneous TG-DSC thermal analyzer (Mettler Toledo, Germany), in the temperature range of $30\text{--}1000^\circ\text{C}$ with a heating rate of $10^\circ\text{C}/\text{min}$ in a nitrogen atmosphere. Based on the results of thermal analysis, mixture of raw materials for all the compositions were calcined in alumina

crucible at 1100°C for 12 h. The calcined powders were mixed with 2 wt% polyvinyl alcohol (PVA) and shaped into cylindrical pellets with diameter ~12 mm and thickness ~ 2mm under a load of 5 tons using a hydraulic press. These pellets were sintered at 1200 °C using a high temperature programmable muffle furnace (Matrix, India) for 12 h. Initially, pellets were heated slowly at a rate of 2 °C/min up to 200 °C and kept at this temperature for 2 h to ensure the complete burning of the binder. Subsequently, the pellets were heated at a rate of 5 °C/min to the sintering temperature, 1200 °C and maintained at this temperature for 12 h, thereafter cooled down to room temperature with a cooling rate 5 °C/min.

2.2 Characterization of materials

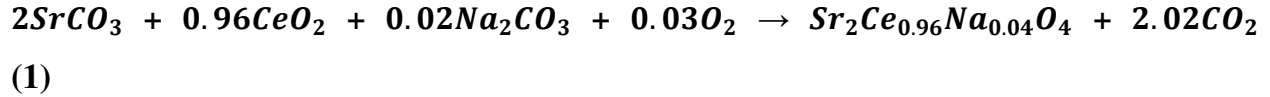
To obtain information about phase formation and crystal structure of the samples, the powder X-ray diffraction pattern of the calcined powders were recorded at room temperature using powder X-ray diffraction (Miniflex II, Rigaku, Japan). The X-ray diffraction patterns of the samples were collected over a wide range of Bragg's angles ($20^\circ < 2\theta < 80^\circ$) using CuK α radiation ($\lambda \approx 1.5406 \text{ \AA}$ and step size of $\Delta 2\theta = 0.02^\circ$) and Ni filter at a scanning rate of 2 °C/min. To detect the presence of impurity phases, Raman spectrum in a wide wave number range 100 – 2000 cm⁻¹ was recorded using the Raman spectroscope (T64000, Jovin-Yvon Horiba, France). Fourier transform of infrared (FTIR) spectrum of the powders was recorded in wave number range 400-4000 cm⁻¹ by the spectroscope (Shimadzu, Model DF 803, Japan) using KBr pellet method. The UV – visible spectrum of the sample was collected in the range of wavelength 150 - 1000 nm in absorption mode by the spectrometer (V-770, Jasco, Japan). The photoluminescence (PL) excitation and emission spectra of the samples were recorded by employing a spectrofluorophotometer (4500, Hitachi, Japan). The microstructure and chemical composition of fractured surfaces of the sintered pellets were examined using Scanning Electron Microscope (EVO18, Zeiss, Japan).

3 Results and Discussion

3.1 Thermal analysis (TG/DSC) of mixture of raw materials

The thermogravimetric (TG) and differential scanning calorimetric (DSC) curves of mixture of raw materials for the samples were recorded in the temperature range 40-1000°C.

Thermogravimetric (TG) and differential scanning calorimetry (DSC) curves for one of the representative samples S2CN4 ($\text{Sr}_2\text{Ce}_{0.96}\text{Na}_{0.04}\text{O}_4$) are shown in Fig. 1 (a). Similar curves were obtained for other samples also. The TGA curve shows a small weight loss in the temperature range 30-100°C which is assigned to dehydration of $\text{Na}_2\text{CO}_3 \cdot \text{H}_2\text{O}$ to Na_2CO_3 . The weight loss (18.88 %) seen in the temperature range 800-900°C may be assigned to the formation of solid solution $\text{Sr}_2\text{Ce}_{0.96}\text{Na}_{0.04}\text{O}_4$ as per the equation (1):



The weight loss calculated theoretically according to the equation (1) is 19.02% which is approximately equal to experimentally calculated weight loss 18.88%. DSC curve shows only one endothermic peak between 900 - 950 °C. This peak is attributed to solid state reaction among the raw materials to form $\text{Sr}_2\text{Ce}_{0.96}\text{Na}_{0.04}\text{O}_4$ (S2CN4) according to equation (1). To fix the calcination temperature TG data were replotted in form of derivative thermogravimetric (DTG) and shown in Fig. 1(b). The DTG curve reveals a peak centered at 909°C exactly at the same temperature at which endothermic peak is recorded in the DSC curve. Based on the results of the thermal analysis it was decided to fix the calcination temperature at 1100 °C. To study the effect of concentration of dopant (Na^{1+}) on the structural and optical properties, calcination temperature for other samples was also kept the same.

3.2 Phase analysis and structural characterization using XRD

The room temperature X-ray diffraction (XRD) pattern of the powders obtained on calcination at 1100 °C for 12 h are illustrated in Fig. 2(a). The observed peaks in the XRD pattern of the samples were indexed using JCPDS file (No. 89-5546) available in the literature for orthorhombic Sr_2CeO_4 [35]. Absence of any extra peak in the XRD pattern of doped samples ruled out the presence of any noticeable impurity phase. To ensure the incorporation of Na^{1+} ions at Ce^{4+} sites of Sr_2CeO_4 , the highest intensity peak corresponding to (130) reflection plane is plotted on an expanded scale and shown in Fig. 2(b). It is noted that the position of this peak for the composition with $x=0.02$ (S2CN2) has shifted towards lower angle (2θ) side as compared to the position of the same peak for the undoped sample S2CN0. But on further increase in the concentration of dopant (Na^{1+}), a systematic reversal trend (towards higher angle side) in shifting

of the position of peak (130) has noticed. It is well known that the shift in the position of XRD peaks depends on the difference in the ionic radius of the dopant and host. In Sr_2CeO_4 , coordination number of both Sr and Ce ions is six. The ionic radius of Sr^{2+} , Ce^{4+} and Na^{1+} ions in coordination number six is 1.18 Å, 0.87 Å and 1.02 Å, respectively. The ionic radius of Na^{1+} is smaller than the ionic radius of Sr^{2+} and larger than the ionic radius of Ce^{4+} . Thus, the peaks in XRD patterns shift towards higher angle (contraction of unit cell dimensions) or lower angle side (expansion in unit cell dimensions) when Na^{1+} ions substitute at Sr-sites or Ce-sites of Sr_2CeO_4 , respectively. The reversal trend of the peak position from lower angle side to higher angle side on increasing doping concentration can be justified by speculating that in the samples with $x=0.04, 0.06$ and 0.10 , Na^{1+} ions are substituted at both Sr^{2+} and Ce^{4+} sites. For the solid solutions Hume-Rothery rules applied on dopant and host elements are: (i) difference in the atomic radius must be within 15%, (ii) the two elements must have same crystal structure, (iii) must have similar electronegativity values and (iv) the two elements must have the same valencies [36]. The percentage of difference in ionic radii (D_r) between host and doped can be calculated by an equation given below [37]:

$$D_r = \frac{R_h(\text{CN}) - R_d(\text{CN})}{R_h(\text{CN})} \times 100 \quad (2)$$

where R_h and R_d are radius of host and dopant ions, respectively while co-ordination number is abbreviated as CN. Value of D_r was calculated by considering Na^{1+} as dopant for (i) Ce^{4+} site and (ii) Sr^{2+} site of Sr_2CeO_4 . The value of D_r for the case (i) is 17.24 while for case (ii) it is 13.56. Furthermore, electronegativity of Na^+ , Sr^{2+} and Ce^{4+} is 0.93, 0.95 and 1.12, respectively. The crystal structure of Na is body center cubic (bcc), Sr is face center cubic (fcc) and Ce double hexagonal. All the information clearly indicate that occupancy of Na^{1+} ions at the Sr^{2+} sites is favorable over the Ce^{4+} sites in the lattice of Sr_2CeO_4 . Studies carried out by earlier researchers on rare earth ions and Na^+ (as charge compensator) co-doped Sr_2CeO_4 phosphors have also shown that Na^{1+} ions prefer to occupy Sr^{2+} sites than Ce^{4+} sites in Sr_2CeO_4 [34]. In our studies of Na^{1+} doped $\text{Sr}_2\text{Ce}_{1-x}\text{Na}_x\text{O}_4$ systems, we observed that the XRD peak corresponding to plane (130) switches from right to left for sample S2CN2 ($x = 0.02$) to S2CN4 ($x = 0.04$). Thus, it can be concluded that the solubility of Na^{1+} at Ce^{4+} site of Sr_2CeO_4 is limited and in the present studies it lies between 2-4 mole%. Structural parameters of the samples were obtained by

performing Rietveld refinement of the XRD patterns using FullProf Suite software package. Structural refinement was carried by adopting orthorhombic structure and space group Pbam of Sr₂CeO₄. The XRD patterns were refined for lattice parameters, scale factor, backgrounds, pseudo-Voigt profile function (u, v and w), atomic coordinates and overall isothermal temperature factors (B_{iso}). Fig. 3 shows the difference between experimentally observed and theoretically calculated XRD patterns. There is a good matching between the observed and calculated patterns which implies that substitution of Na¹⁺ in the lattice of Sr₂CeO₄ has not induced any structural transition. The value of lattice parameters and unit cell volume are given in Table 1. The crystal structure of all the compositions was modeled by VESTA program using the Rietveld refined structural parameters, and the typical unit cell and coordination environment of Sr and Ce atoms in Sr₂CeO₄ (S2CN0) is also shown in Fig. 3 (right bottom). It is clear from the Fig. 3 that the structure of Sr₂CeO₄ consists of linear chains of edge-sharing CeO₆ octahedral. In these chains there are two terminal Ce-O_I groups perpendicular to the plane defined by four equatorial O_{II} atoms. The terminal Ce-O_I bonds are approximately 0.1 Å shorter than the equatorial bonds.

The crystallite size of the powders is generally calculated using Debye-Scherrer's method is not considered to be accurate because the line broadening may also have a contribution due to microstrain. In the literature Size Strain Plot (SSP) method has been used to evaluate the crystallite size and microstrain [38]. The advantage of this method is that it gives less weightage to the data of reflection arises from higher angles where precession is lower. Therefore, Size Strain Plot (SSP) method has been used to determine the crystallite size and microstrain the samples. As per the SSP plot method, interplanar spacing and microstrain is related according to equation (3):

$$\left(\frac{d_{hkl}\beta\cos\theta}{\lambda}\right)^2 = \frac{k\lambda}{D} \left(\frac{d_{hkl}^2\beta\cos\theta}{\lambda^2}\right) + \left(\frac{\varepsilon}{2}\right)^2 \quad (3)$$

where, d_{hkl} is the interplanar spacing corresponding to the plane (hkl), k , λ , and D are the same as mentioned in equation (3) and ε is the average strain generated in the lattice. The plot of

$\left(\frac{d_{hkl}\beta\cos\theta}{\lambda}\right)^2$ vs. $\left(\frac{d_{hkl}^2\beta\cos\theta}{\lambda^2}\right)$ for all the samples are shown in Fig.4. By linear fitting of the

experimental data points, the value of slope and intercept were obtained. The value of crystalline size is determined by value of the slope whereas square root of the intercept on y-axis provides the value of lattice strain. The value of crystallite size and lattice strain of different compositions are mentioned in Table 1. From the Table 1, it is observed that crystallite size of doped samples is slightly larger as compared to undoped sample. Further, it is noticed that value of micro strain increases with increasing concentration up to $x=0.04$ (S2CN4), further increase in the doping concentration leads to the decrease in the value of micro strain. The decrease in the value of micro strain for higher doping concentration samples is possible when Na^{1+} ions substitute Sr^{2+} ions rather than Ce^{4+} ions in Sr_2CeO_4 . It is already mentioned above that mismatch in ionic radii and valence state of Sr^{2+} and Na^{1+} is large as compared to Ce^{4+} and Na^{1+} . The values of micro strain given in the table are in agreement with values reported for Ho doped $\text{Sr}_{2-x}\text{Ho}_x\text{CeO}_4$ system [37].

3.3 Raman spectrum analysis

In the last two decades many researchers have focused their attention on synthesizing Sr_2CeO_4 oxide by different possible methods [39–43]. These studies have demonstrated that obtaining phase pure powder of Sr_2CeO_4 oxide by any methods is challenging. The common impurities phases found in the powder of Sr_2CeO_4 are SrCeO_3 , SrCO_3 , CeO_2 [44,45]. The major XRD diffraction peaks of these impurity phases overlap with diffraction peaks of Sr_2CeO_4 , hence it is difficult to detect these impurity phases by XRD. Beside this difficulty, the conventional XRD technique has low limit ($\geq 5\%$) for the detection of purity phases. Therefore, one cannot rely only on the XRD results to confirm the purity of the synthesized powders. From the literature it was found that Raman spectrum of Sr_2CeO_4 is completely different than the Raman spectrum of above-mentioned impurities phases particularly of SrCeO_3 [46]. Moreover, sensitivity of Raman spectroscopy is higher than the conventional XRD technique. Thus, to cross check the purity of the synthesized powders, room temperature Raman spectra in the wave number range $80\text{-}800\text{ cm}^{-1}$ were recorded and depicted in Fig. 5(a). The Raman spectrum of all the samples is very much similar to the Raman spectrum of Sr_2CeO_4 reported by earlier workers [47]. Two intense bands around 287 and 386 cm^{-1} are seen in the Raman spectrum of all the samples. Based on the information available in the literature, the bands around 287 cm^{-1} and 386 cm^{-1} are assigned to the stretching modes $\text{Ce}-\text{O}_{\text{II}}$ (equatorial) and $\text{Ce}-\text{O}_{\text{I}}$ (terminal), respectively

of CeO_6 octahedral in Sr_2CeO_4 [48]. On careful observation of the spectra it is found that the change in the position of these bands from sample S2CN0 ($x=0.00$) to S2CN10 ($x=0.10$) is almost negligible. On the other hand, a systematic, measurable change in the intensity and full width at half maxima (FWHM) of the band observed at 287 cm^{-1} (as shown in Fig. 5 (b)) is seen. The intensity of the band is highest, and FWHM is lowest for the composition with $x=0.04$ (S2N4) which confirms the least distorted/defective structure of this sample in agreement with XRD results. In the Raman spectrum of the composition with $x = 0.10$ a few extra bands are seen (marked with * in Fig.5 (a)) which corresponds to SrCeO_3 phase [46]. From the analysis of XRD results it has become clear that in the composition with $x=0.10$ (S2CN10) most of the Na^{1+} ions occupy Sr^{2+} sites. When Na^{1+} ions occupy Sr^{2+} sites instead of designated Ce^{4+} sites, the Ce sites in the lattice of Sr_2CeO_4 remain vacant (V_{Ce}). Presence of large number of cerium vacancies can reduce the stability of Sr_2CeO_4 structure leading to its decomposition according to the reaction $\text{Sr}_2\text{CeO}_4 \rightarrow \text{SrCeO}_3 + \text{SrO}$. Due to similar diffraction pattern of SrCeO_3 and Sr_2CeO_4 , XRD could not able to detected the presence of SrCeO_3 . Another reason for not detection of SrCeO_3 phase using XRD is that the amount of SrCeO_3 phase in the powder of S2CN10 sample should be below the detection limit of the XRD. No Raman bands of starting materials SrCO_3 , CeO_2 and Na_2O were detected in the spectrum which is in agreement with XRD result.

3.4 Fourier Transform Infrared (FTIR) Analysis

It is reported in the literature that FTIR can detect the impurity of alkaline earth metals carbonate (SrCO_3 and BaCO_3) upto 0.6 % [49]. Therefore, to detect the presence of impurity phase SrCO_3 in the synthesized powders, FTIR analysis was carried out. Fig.6 shows the FTIR spectra of the samples in the wave number range $450\text{-}4000\text{ cm}^{-1}$. The spectrum of doped samples is similar to the spectrum of undoped sample. It is reported in the literature that presence of bands between $400 - 600\text{ cm}^{-1}$ in the FTIR spectrum confirm the formation of Sr_2CeO_4 structure [50]. The FTIR spectra of the samples also a band below 500 cm^{-1} is seen but due to the limitation of FTIR spectrometer used in this work complete band could not be recorded. Beside this characteristic band, spectrum of all the samples contain one two strong intensity band around 858 cm^{-1} and 1450 cm^{-1} which are characteristic band of SrCO_3 [51]. Presence of these SrCO_3 bands in the FTIR spectrum contradicts the XRD and Raman results in which no peak and bands

of SrCO₃ were detected. The reason for not detection of SrCO₃ impurity phase by the XRD and Raman techniques could be its existence in the amorphous phase.

A weak intensity broad band in the in the wave number range 3400-3500 cm⁻¹ is also seen in the spectra. This broad band is attributed to the physically adsorbed H₂O [12] on the surface of particles from the moisture present in the atmosphere. A few very weak intensity bands were also observed which originate due to vibration of atoms in CO₂ or H₂O molecules.

3.5 UV-Visible Spectrum Analysis

In order to estimate the optical band gap of the synthesized samples, UV spectrum (in absorbance mode) has been recorded in the wavelength range 150-1000 nm as shown in Fig.7. In the UV spectra strong absorption band below 450 nm is observed in the spectrum of all the samples. On substitution of Na¹⁺, the position of the absorption maxima has initially shifted towards higher wavelength side upto x = 0.04 (S2CN4) and on further increase in the doping concentration absorption band shifts towards lower wavelength. Among all the samples, sample S2CN2 (x=0.02) has the highest intensity of absorption band. Further it is observed in the visible range absorption of doped samples (for S2CN4 it is 14 %) is higher that undoped sample (for S2CN0 it is 3 %). To estimate the value of optical band gap, the absorbance data shown in Fig. 7 were plotted according to Tauc equation (5) [52];

$$(\alpha h\nu)^{1/m} = A(h\nu - E_g) \quad (5)$$

Here α is the absorption coefficient, h is the Planck's constant, ν is the frequency of incident light, A is the constant, and E_g is the optical band gap energy. The value of exponent m indicates the nature of the optical transitions. The value $m = 1/2, 2, 1.5$ and 3 corresponds to the direct allowed, indirect allowed, direct forbidden and indirect forbidden transitions, respectively. The Tauc plots for the direct allowed transition ($m=1/2$) were generated and shown in Fig. 8. The value of band gap energy was obtained from the linear fitting at the inflection point of $(\alpha h\nu)^{1/m}$ versus $h\nu$ plots shown in Fig. 8. The obtained values of band gap energy are listed in Table 1. The value of optical band gap for undoped sample S2CN0 (Sr₂CeO₄) is in agreement with the reported values [53]. From the Table 1 it is noted that value of optical band gap energy decreases with increasing doping concentration. The decrease in the value of band gap energy can be

attributed to widening of the acceptor (Na) band on account of increasing concentration and finally mixing with the valence band.

3.6 Photoluminescence Studies

Fig. 9 shows the photoluminescence excitation (PLE) spectra of the samples recorded at room temperature by fixing emission wavelength at 467 nm. Photoluminescence spectrum of the sample S2CN10 was not recorded due to the presence of impurity phases in the calcined powder of this sample (as confirmed from the Raman spectrum analysis). In the excitation spectra two well resolved bands, one in the range 290-297 nm (high energy) and the other in the range 341-362 nm (low energy) are seen. The exact position and intensity of these bands are depicted in Table 2. The position of excitation bands 290 and 337 nm observed for undoped sample Sr_2CeO_4 is almost the same as reported by earlier workers [11]. The structure of Sr_2CeO_4 is built up by edge-sharing CeO_6 octahedra. Two terminal Ce-O_I bonds are 0.1 Å shorter than the four equatorial bands Ce-O_{II}. Thus, two bands observed in the excitation spectra may be related to two different Ce-O bond lengths in the lattice. The bands centred at 290 and 337 nm are attributed to the charge transfer band (CTB) caused by an electron transfer from the O_2 (2p) orbital to the empty states of the $4f^6$ configuration of Ce^{4+} (Ce^{4+} -O). The higher energy band (at 290nm) originated due to transition from terminal oxygen (O_I) to Ce^{4+} . The low energy band (at 340 nm) is ascribed to the transition of an electron from equatorial oxygen (O_{II}) to Ce^{4+} [11]. It is noted from the table 2 that on Na^+ doping the position of both the bands has shifted towards higher wavelength side. The shift in the low wavelength (high energy) band is 7nm for the sample S2CN4 which is negligible. On the other hand, shift in the position of higher wavelength (low energy) band is 25 nm observed for the sample S2CN2. As it is mentioned above that low energy band corresponds to transition of an electron from equatorial (O_{II}) oxygen to Ce^{4+} , thus it can be concluded that environment of equatorial oxygen has affected more as compared to terminal oxygen.

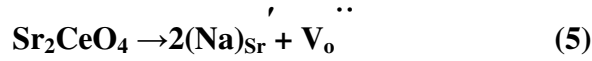
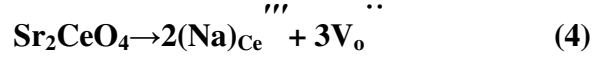
From the Fig. 9 and table 2, it is observed that for undoped sample the intensity of high energy (lower wavelength) band is higher as compared to low energy (higher wavelength) band which is in agreement with results published by earlier researcher. Contrary to this observation in all Na^{1+} doped samples the intensity of low energy band is higher than that of high energy band. For the sample S2CN2 ($x=0.02$) the intensity of low energy excitation band is 3.5 times

than the intensity of high energy band. In almost all the studies carried out by earlier workers related to excitation spectrum of undoped and Sr site doped Sr_2CeO_4 oxides, intensity of high energy band is always higher than the low energy band. Even in the system $\text{Sr}_2\text{Ce}_{1-x}\text{M}_x\text{O}_4$ (M=Er, Yb and Nd) also this trend is maintained [23,29,30]. But one study in which Sn is substitute at Ce site i.e in the system $\text{Sr}_2\text{Ce}_{1-x}\text{Sn}_x\text{O}_4$, the intensity of the low energy band is higher than that of the high energy band for $x=0.07$. The authors ascribed enhanced excitation intensity of the low energy peak to weak crystal field because crystal field is highly sensitive to ionic radius and nature of the dopants [31]. The weak crystal field leads to more electrons transferring from equatorial oxygen (O_{II}) to Ce^{4+} than from terminal oxygen (O_I) to Ce^{4+} .

The excitation spectrum studies show that the emission spectrum can be recorded under the excitation by 337 nm source. Therefore, the photoluminescence emission spectrum of all the samples has been recorded using excitation wavelength $\lambda_{ex} = 337 \text{ nm}$ and shown in Fig. 9(b).

The shape of PL emission spectrum of Na^{1+} doped samples and undoped sample remains practically similar having a broad band in 400-750 nm range, peak centred at 472 nm. Further, it was observed that band is asymmetric in high wavelength range. Similar kind of broad band PL spectrum for Sr_2CeO_4 has been reported by Danielson et al. and other researchers [4]. The single broad band emission band is attributed to the emission from two ligand metal charge transfer (LMCT) states. To confirm this value of the Stokes shift was calculated by the difference between the low energy excitation peak (337 nm) and the emission maximum (472 nm). The value of Stokes shift for all the samples is listed in Table 2. A typical Stokes shift for a charge transfer transition on a rare earth ion ranges from 4000 cm^{-1} to $17,000 \text{ cm}^{-1}$ [54,55]. The Stokes shift of the synthesized samples fits very well in the range expected for charge transfer transitions. Further, it is noticed that with the incorporation Na^{1+} ions, no extra absorption states are observed. Value of peak maximum and intensity of the emission for the samples are listed in Table 2. From the table 2, it is found that intensity of the emission spectrum has reduced significantly for the composition with $x=0.02$ (S2CN2) thereafter on further increase in the doping concentration (for sample S2CN4 and S2CN6) an improvement in the intensity is recorded. The two possible reasons for the reduced intensity on doping Na^+ are: (i) energy transfer from $\text{Ce}^{4+}\text{-O}^{2-}$ to $\text{Na}^+\text{-O}^{2-}$ and (ii) presence of considerable amount of oxygen vacancies. Reason (i) is ruled out because with increasing doping concentration reduction in the intensity

has to continue upto the highest concentration sample S2CN6 but it is not observed experimentally. When Na⁺ ions substitute at Sr²⁺ and Ce⁴⁺ sites of Sr₂CeO₄, charge neutrality condition is maintained by the formation of oxygen vacancies. Mechanism of the formation of oxygen vacancies are written in Kröger Vink's notation according to equations (3) and (4);



It is quite obvious that number of oxygen vacancies per dopant (Na¹⁺) ion for the site Ce⁴⁺ sites is 1.5 whereas for Sr²⁺ sites is 0.5. As it is mentioned above that emission in these samples originate due to energy transfer from Ce⁴⁺ to O²⁻, thus decreases in the concentration of O²⁻ (formation of oxygen vacancies) would weaken the charge transfer process resulting into reduction in the intensity of emission. Studies of photo luminance properties of CeO₂ have demonstrated that high concentration of oxygen vacancies acts as luminescence quencher [56]. The significant reduction in the emission intensity of sample S2CN2 is again an indication of incorporation of Na¹⁺ ions completely on Ce⁴⁺ sites whereas in samples S2CN4 and S2CN6 partially on Sr²⁺ and partially on Ce⁴⁺ sites or may be completely on Sr²⁺ sites.

The effect of Na⁺ doping on PL emission spectrum of Sr₂CeO₄ has been studied by determining CIE chromaticity coordinates x and y. The CIE co-ordinates calculated by the Spectrophotometric method using the spectral energy distribution of the Sr₂CeO₄ sample are shown in Fig.9 (c). The color co-ordinates for the all the samples are given in Table 2. No obvious change in the x and y co-ordinates was noted even for the highest dopant concentration sample S2CN6. The colour co-ordinates for the pure Sr₂CeO₄ were x = 0.17 and y = 0.25 as given in the table 2, slightly mismatch with the co-ordinates reported by Danielson et al. (x=0.20, y= 0.30) [4] but it agrees with Jiang et al. (x= 0.19, y = 0.26) [19]. A schematic diagram representing different energy states and corresponding processes for two samples S2CN0 and S2CN2 is shown in Fig.10.

3.7 Microstructural Analysis

In order study the effect of dopant Na¹⁺ on the surface morphology of Sr₂CeO₄, scanning electron micrographs of the fractured surfaces of the pellets sintered at 1200 °C for 8 h were recorded and shown in Fig.11. It is observed from the SEM images of the samples that

morphology of grains is different for different samples. The shape of grains of undoped sample (S2CN0) is polyhedral with sharp edges in agreement with previous reports [26]. The micrograph of the sample S2CN2 contains well developed grains of different sizes and clearly visible clean grain boundaries. The micrograph of sample S2CN4 contains hard grains of large sized and irregular shaped. The shape of grains in the microstructure of sample S2CN6 is abnormal and appear partially melted. In the microstructure of sample S2CN10, presence of secondary phase may be SrCeO_3 is clearly visible. Beside this feature few cracks and voids are also seen in the micrograph. It necessary to mention here that in this work mixture of raw materials were calcined at 1100°C for 8 h. The melting temperature of Na_2O is 1133°C , therefore a small amount of Na_2O may be in the molten state and play the role of flux to promote the host lattice formation and grain growth. The flux in molten form improves the sintering process and promote the grain growth with the liquid sintering mechanism. On account of limited solubility of Na^{1+} ions in the lattice of Sr_2CeO_4 at both Sr^{2+} and Ce^{4+} sites, and in the sample S2CN10, excess Na_2O segregated at the grain boundaries and hindered grain to grain contact. It is worthwhile to mention here that, sintered pellets of the samples S2CN10 collapsed into powder form within a week of sintering. The grain size of other samples calculated using Image J software using linear intercept method lies between 2 – 5 μm .

4 Conclusion

Thermal analysis of mixture of raw material for the sample S2CN4 suggested calcination of mixture $\geq 910^\circ\text{C}$. Based on the results of thermal analysis, powders of a few compositions of the system $\text{Sr}_2\text{Ce}_{1-x}\text{Na}_x\text{O}_4$ ($x=0.00, 0.02, 0.04, 0.6$ and 0.10) were obtained by calcination at 1100°C for 8 h. The XRD pattern analysis indicated limited solubility (between 2-4 mole %) of Na^{1+} at Ce^{4+} site of Sr_2CeO_4 . In higher compositions samples S2CN6 and S2CN10, occupancy of Na^{1+} at Sr^{2+} sites are also observed. The Rietveld refinement of the XRD pattern of the samples confirmed that Na doped samples have orthorhombic structure and space group Pbam similar to undoped sample Sr_2CeO_4 . Purity of the synthesized samples was checked using Raman technique and found that powder of sample S2CN10 is contaminated with impurity phase SrCeO_3 . The FTIR spectrum analysis indicated presence of SrCO_3 in the powder. UV-visible studies suggested a decrease in the band gap energy from 3.10 – 2.95 eV with increasing doping concentration. Two well resolved bands were observed in the excitation photoluminescence

spectrum of all the samples. But intensity of low energy band is highest for the sample S2CN2 making this material potential candidate for infrared excitation source. In the emission photoluminescence spectrum of all the sample a broad band centered around 470 nm is seen. The intensity emission band is lowest for the sample S2CN2 which is attributed to excess number of oxygen vacancies in this sample. Further, it is concluded that an optimum number of oxygen vacancies can improve the intensity of emission band. The scanning electron microscopes (SEM) studies have confirmed a key role of the dopant Na^{1+} in the development of microstructure. For further confirmation of the experimental results obtained in this work, synthesis and characterization of few compositions of the system $\text{Sr}_{2-x}\text{Na}_x\text{CeO}_4$ are required.

Acknowledgements

The authors are grateful to Prof. R.K. Singh, Department of Physics, Institute of Science, Banaras Hindu University (BHU), Varanasi, India for providing Raman Facility. Mr. Dharmendra Yadav and Gurudeo Nirala are thankful to the Ministry of Human Resource and Development (MHRD), Government of India for the financial assistantship as Senior Research Scholar Fellowship (SRF).

References

- [1] Höpfe, H. A. (2009). Recent developments in the field of inorganic phosphors. *Angewandte Chemie International Edition*, 48(20), 3572-3582.
- [2] Xia, Z., Ma, C., Molokeev, M. S., Liu, Q., Rickert, K., & Poeppelmeier, K. R. (2015). Chemical unit cosubstitution and tuning of photoluminescence in the $\text{Ca}_2(\text{Al}_{1-x}\text{Mg}_x)(\text{Al}_{1-x}\text{Si}_{1+x})\text{O}_7:\text{Eu}^{2+}$ phosphor. *Journal of the American Chemical Society*, 137(39), 12494-12497.
- [3] Lacanilao, A., Wallez, G., Mazerolles, L., Buissette, V., Le Mercier, T., Aurissergues, F., ... & Viana, B. (2013). A structural approach of the flux effect on blue phosphor BAM: Eu ($\text{BaMgAl}_{10}\text{O}_{17}:\text{Eu}^{2+}$). *Materials Research Bulletin*, 48(8), 2960-2968.
- [4] Danielson, E., Devenney, M., Giaquinta, D. M., Golden, J. H., Haushalter, R. C.,

- McFarland, E. W., ... & Di Wu, X. (1998). A rare-earth phosphor containing one-dimensional chains identified through combinatorial methods. *Science*, 279(5352), 837-839.
- [5] Li, L., Zhou, S., & Zhang, S. (2008). Investigation on charge transfer bands of Ce⁴⁺ in Sr₂CeO₄ blue phosphor. *Chemical Physics Letters*, 453(4-6), 283-289.
- [6] Stefanski, M., Lukaszewicz, M., Hreniak, D., & Streck, W. (2019). Impact of the synthesis procedure on the spectroscopic properties of anti-Stokes white emission obtained from Sr₂CeO₄ phosphor. *Journal of Photochemistry and Photobiology A: Chemistry*, 382, 111855.
- [7] Yang, Y., Zuo, X., Shi, S., Li, J., Wang, J., Geng, L., & Fu, L. (2019). Hydrothermal combustion synthesis and characterization of Sr₂CeO₄ phosphor powders. *Materials Research Bulletin*, 112, 159-164.
- [8] Nirala, G., Yadav, D., & Upadhyay, S. (2020). Ruddlesden-Popper phase A₂BO₄ oxides: Recent studies on structure, electrical, dielectric, and optical properties. *Journal of Advanced Ceramics*, 1-21.
- [9] Dejene, F. B. (2018). Thermoluminescence study of beta irradiated Sr₂CeO₄: Eu³⁺ phosphor synthesized using solution-combustion process. *Journal of Luminescence*, 199, 433-441.
- [10] Kato, T., Kawano, N., Okada, G., Kawaguchi, N., Koshimizu, M., & Yanagida, T. (2019). Scintillation and photoluminescence properties of Sr₂CeO₄ ceramics. *Optical Materials*, 87, 139-144.
- [11] Zhang, C., Jianshe, S., Xujie, Y., Lude, L., & Xin, W. (2010). Preparation, characterization and luminescence of Sm³⁺ or Eu³⁺ doped Sr₂CeO₄ by a modified sol-gel method. *Journal of Rare Earths*, 28(4), 513-518.
- [12] Monika, D. L., Nagabhushana, H., Krishna, R. H., Nagabhushana, B. M., Sharma, S. C., & Thomas, T. (2014). Synthesis and photoluminescence properties of a novel Sr₂CeO₄: Dy³⁺ nanophosphor with enhanced brightness by Li⁺ co-doping. *RSC advances*, 4(73),

38655-38662.

- [13] Zhou, R., Wei, X., Chen, Y., Duan, C., & Yin, M. (2012). Ultraviolet to near-infrared downconversion in Yb³⁺-doped Sr₂CeO₄. *physica status solidi (b)*, 249(4), 818-823.
- [14] Rakov, N., Guimaraes, R. B., & Maciel, G. S. (2011). Strong infrared-to-visible frequency upconversion in Er³⁺-doped Sr₂CeO₄ powders.
- [15] Gupta, S. K., Sahu, M., Krishnan, K., Saxena, M. K., Natarajan, V., & Godbole, S. V. (2013). Bluish white emitting sr₂ ceo₄ and red emitting sr₂ ceo₄: Eu³⁺ nanoparticles: Optimization of synthesis parameters, characterization, energy transfer and photoluminescence. *Journal of Materials Chemistry C*, 1(42), 7054-7063.
- [16] Li, Q., Liu, Z. P., Li, X. J., & Dong, L. M. (2016). Synthesis and Luminescence properties of Sr₂CeO₄: Eu³⁺, Tb³⁺ phosphors. *dig. J. Nonmaterials Biostructures Nonmaterials Biostructures*, 11, 313-319.
- [17] Li, J., Li, X., Hu, S., Li, Y., & Hao, Y. (2013). Photoluminescence mechanisms of color-tunable Sr₂CeO₄: Eu³⁺, Dy³⁺ phosphors based on experimental and first-principles investigation. *Optical Materials*, 35(12), 2309-2313.
- [18] Suresh, K. M. K. A., Murthy, K. V. R., Rao, C. A., Rao, N. P., & Rao, B. S. (2013). Synthesis and characterization of nano Sr₂CeO₄ doped with Eu and Gd phosphor. *Journal of luminescence*, 133, 96-101.
- [19] Jiang, Y. D., Zhang, F., Summers, C. J., & Wang, Z. L. (1999). Synthesis and properties of Sr₂CeO₄ blue emission powder phosphor for field emission displays. *Applied physics letters*, 74(12), 1677-1679.
- [20] Park, C. H., Kim, C. H., Pyun, C. H., & Choy, J. H. (2000). Luminescence of Sr₂CeO₄. *Journal of luminescence*, 87, 1062-1064.
- [21] Li, J., Wang, L., Zhou, H., Liu, X., & Xu, B. (2010). Electronic properties and europium ion photoluminescence behaviors in Sr₂CeO₄ phosphor. *Journal of alloys and compounds*, 506(2), 950-955.

- [22] Strek, W., Tomala, R., Marciniak, L., Lukaszewicz, M., Cichy, B., Stefanski, M., ... & Seijo, L. (2016). Broadband anti-Stokes white emission of Sr₂CeO₄ nanocrystals induced by laser irradiation. *Physical Chemistry Chemical Physics*, 18(40), 27921-27927.
- [23] Stefanski, M., Lukaszewicz, M., Hreniak, D., & Strek, W. (2017). Broadband laser induced white emission observed from Nd³⁺ doped Sr₂CeO₄ nanocrystals. *Journal of Luminescence*, 192, 243-249.
- [24] Joaquim, F. L., Rocha, L. A., Júnior, C. S. N., Esbenshade, J., Schiavon, M. A., & Ferrari, J. L. (2019). In situ temperature effect on spectral downshifting emission on Er³⁺ doped-Sr₂CeO₄ photoluminescent materials. *Journal of Alloys and Compounds*, 774, 694-699.
- [25] Stefanski, M., Lukaszewicz, M., Hreniak, D., & Strek, W. (2017). Laser induced white emission generated by infrared excitation from Eu³⁺: Sr₂CeO₄ nanocrystals. *The Journal of Chemical Physics*, 146(10), 104705.
- [26] Yadav, D., Kumar, U., & Upadhyay, S. (2019). Study of structural, electrical, and photoluminescent properties of SrCeO₃ and Sr₂CeO₄. *Journal of Advanced Ceramics*, 8(3), 377-388.
- [27] Gorelov, V. P., Balakireva, V. B., & Vorotnikov, V. A. (2019). Proton Conductivity of Acceptor-Doped Sr₂CeO₄. *Inorganic Materials*, 55(11), 1167-1171.
- [28] Beshkar, F., Amiri, O., Salehi, Z., & Salavati-Niasari, M. (2018). Surfactant free synthesis of Sr₂CeO₄ nanostructures and their application in removal of organic pollutions. *Journal of Materials Science: Materials in Electronics*, 29(8), 6978-6984.
- [29] Stefanski, M., Hreniak, D., & Strek, W. (2017). Broadband white emission from Yb³⁺ doped Sr₂CeO₄ nanocrystals. *Optical Materials*, 65, 95-98.
- [30] Seo, Y. W., Moon, B. K., Choi, B. C., Jeong, J. H., Choi, H., & Kim, J. H. (2015). Synthesis and up-conversion luminescence properties of Er³⁺/Yb³⁺ co-doped Sr₂CeO₄ phosphors. *Ceramics International*, 41(10), 14332-14339.
- [31] Hsu, C. H., Liaw, C. L., & Lu, C. H. (2010). Luminescence properties of sol-gel derived Sr₂(Ce_{1-x}Sn_x)O₄ blue phosphors. *Journal of alloys and compounds*, 489(2), 445-450.

- [32] Shi, L., Li, C., & Su, Q. (2011). Investigation on temperature dependence of photoluminescence in $\text{Sr}_{1-x}\text{Eu}_x\text{O}_4$ phosphors. *Journal of alloys and compounds*, 509(11), 4209-4213.
- [33] Xiao, Q., Dong, G., & Qiu, J. (2014). Near-infrared luminescence enhancing by introducing alkali metal ions in Sr_2CeO_4 : Yb^{3+} . *Journal of luminescence*, 147, 163-167.
- [34] Li, H., Jia, Y., Sun, W., Fu, J., Pang, R., & Li, C. (2015). Influence of charge compensators on photoluminescence properties of Sr_2CeO_4 : Eu^{3+} . *Materials Letters*, 139, 258-261.
- [35] Murthy, K. V. R., Rao, B. N., Rajasekhar, B. N., Kumar, B. W. R., Suresh, K., & Rao, B. S. (2012). Effect of Flux on the Formation of Sr_2CeO_4 Phosphor Doped With Er. *Physics Procedia*, 29, 65-69.
- [36] Hume-Rothery, W., & Powell, H. M. (1935). On the theory of super-lattice structures in alloys. *Zeitschrift für Kristallographie-Crystalline Materials*, 91(1-6), 23-47.
- [37] Monika, D. L., Nagabhushana, H., Nagabhushana, B. M., Sharma, S. C., Anantharaju, K. S., Prasad, B. D., & Shivakumara, C. (2015). One pot auto-ignition based synthesis of novel Sr_2CeO_4 : Ho^{3+} nanophosphor for photoluminescent applications. *Journal of Alloys and Compounds*, 648, 1051-1059.
- [38] Kumar, S., Basu, S., Rana, B., Barman, A., Chatterjee, S., Jha, S. N., ... & Ghosh, A. K. (2014). Structural, optical and magnetic properties of sol-gel derived ZnO : Co diluted magnetic semiconductor nanocrystals: an EXAFS study. *Journal of Materials Chemistry C*, 2(3), 481-495.
- [39] Xiao, X., & Yan, B. (2008). Sr_2CeO_4 : Eu^{3+} and Sr_2CeO_4 : 5 mol% Eu^{3+} , 3 mol% Dy^{3+} microphosphors: Wet chemistry synthesis from hybrid precursor and photoluminescence properties. *Journal of Physics and Chemistry of Solids*, 69(7), 1665-1668.
- [40] Yu, X., He, X., Yang, S., Yang, X., & Xu, X. (2004). Synthesis and luminescence of Sr_2CeO_4 superfine particles by citrate-gel method. *Materials Letters*, 58(1-2), 48-50.
- [41] Gomes, J., Pires, A. M., & Serra, O. A. (2004). Morphological study of Sr_2CeO_4 blue

- phosphor with fine particles. *Química Nova*, 27(5), 706-708.
- [42] Kholam, Y. B., Deshpande, S. B., Khanna, P. K., Joy, P. A., & Potdar, H. S. (2004). Microwave-accelerated hydrothermal synthesis of blue white phosphor: Sr₂CeO₄. *Materials letters*, 58(20), 2521-2524.
- [43] Lu, C. H., Wu, T. Y., & Hsu, C. H. (2010). Synthesis and photoluminescent characteristics of Sr₂CeO₄ phosphors prepared via a microwave-assisted solvothermal process. *Journal of luminescence*, 130(5), 737-742.
- [44] Rocha, L. A., Schiavon, M. A., Nascimento Jr, C. S., Guimarães, L., Góes, M. S., Pires, A. M., ... & Ferrari, J. L. (2014). Sr₂CeO₄: Electronic and structural properties. *Journal of alloys and compounds*, 608, 73-78.
- [45] Ferrari, J. L., Pires, A. M., Serra, O. A., & Davolos, M. R. (2011). Luminescent and morphological study of Sr₂CeO₄ blue phosphor prepared from oxalate precursors. *Journal of luminescence*, 131(1), 25-29.
- [46] Yadav, D., Kumar, U., Nirala, G., Mall, A. K., & Upadhyay, S. (2019). Effect of acceptor Na¹⁺ doping on the properties of perovskite SrCeO₃. *Journal of Materials Science: Materials in Electronics*, 30(16), 15772-15785.
- [47] Sahu, M., Gupta, S. K., Jain, D., Saxena, M. K., & Kadam, R. M. (2018). Solid state speciation of uranium and its local structure in Sr₂CeO₄ using photoluminescence spectroscopy. *Spectrochimica Acta Part A: Molecular and Biomolecular Spectroscopy*, 195, 113-119.
- [48] Zhang, C., Jiang, W., Yang, X., Han, Q., Hao, Q., & Wang, X. (2009). Synthesis and luminescent property of Sr₂CeO₄ phosphor via EDTA-complexing process. *Journal of alloys and compounds*, 474(1-2), 287-291.
- [49] Bai, J. G., Creehan, K. D., & Kuhn, H. A. (2007). Inkjet printable nanosilver suspensions for enhanced sintering quality in rapid manufacturing. *Nanotechnology*, 18(18), 185701.
- [50] Guo, H., & Qiao, Y. (2008). Preparation, structural and photoluminescent properties of CeO₂: Eu³⁺ films derived by Pechini sol-gel process. *Applied Surface Science*, 254(7),

1961-1965.

- [51] J.M. Alía, Y. Díaz De Mera, H.G.M. Edwards, P. González Martín, S. López Andrés, (1997). FT-Raman and infrared spectroscopic study of aragonite - Strontianite ($\text{Ca}_x\text{Sr}_{1-x}\text{CO}_3$) solid solution, *Spectrochim. Acta - Part A Mol. Biomol. Spectrosc.* 53, 2347–2362.
- [52] Gao, H., & Wang, Y. (2006). Photoluminescence of Eu³⁺ activated Ba₂SnO₄ under ultraviolet–vacuum ultraviolet excitation. *Journal of materials research*, 21(7), 1857–1861.
- [53] Sudheendra, H. S., Darshan, G. P., Basavaraj, R. B., Naik, Y. V., Premakumar, H. B., Nagabhushana, H., ... & Kokila, M. K. (2019). Influence of Zn²⁺ doping on the lattice defects and photoluminescence studies of Sr₂CeO₄: Eu³⁺ nanophosphor: Applications for data encryption strategies. *Optical Materials*, 90, 159-171.
- [54] Dorenbos, P. (2005). The Eu³⁺ charge transfer energy and the relation with the band gap of compounds. *Journal of luminescence*, 111(1-2), 89-104.
- [55] Choe, J. Y., Ravichandran, D., Blomquist, S. M., Kirchner, K. W., Forsythe, E. W., & Morton, D. C. (2001). Cathodoluminescence study of novel sol–gel derived Y_{3-x}Al₅O₁₂: Tb^x phosphors. *Journal of luminescence*, 93(2), 119-128.
- [56] Kumar, A., Babu, S., Karakoti, A. S., Schulte, A., & Seal, S. (2009). Luminescence properties of europium-doped cerium oxide nanoparticles: role of vacancy and oxidation states. *Langmuir*, 25(18), 10998-11007.

Figures

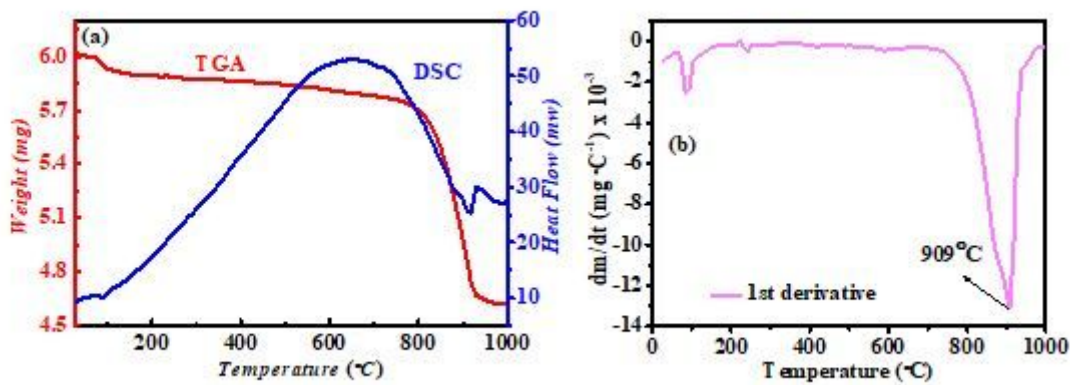


Figure 1

(a) Thermo gravimetric analysis (TGA) & differential scanning calorimetric (DSC) curve and (b) Derivative thermogravimetric curve for the mixture of raw materials for the sample $\text{Sr}_2\text{Ce}_{0.96}\text{Na}_{0.04}\text{O}_4$

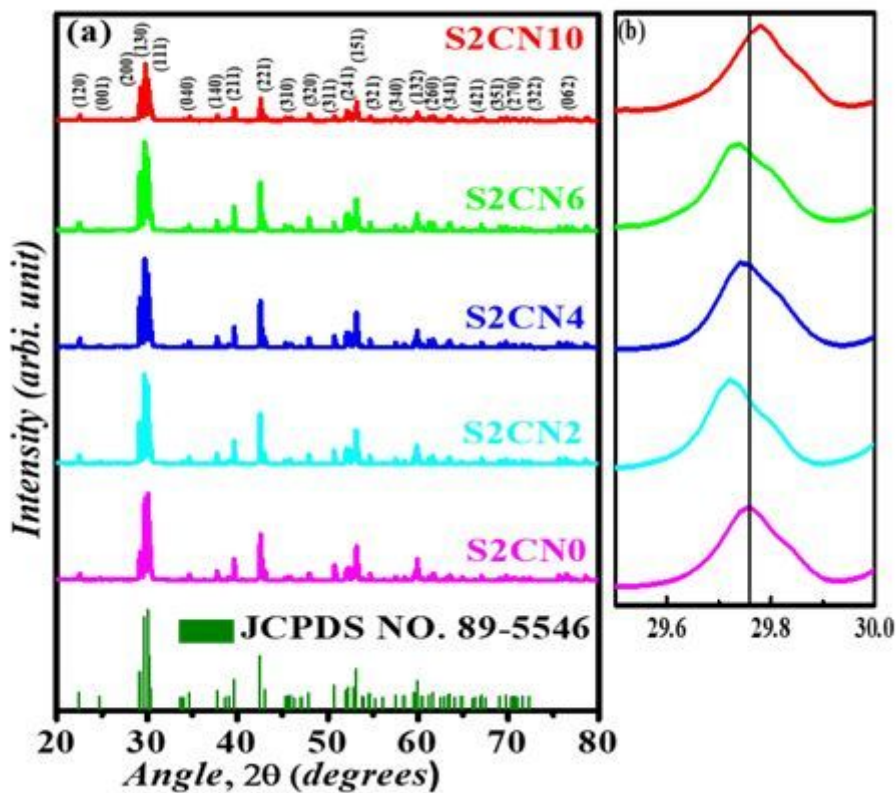


Figure 2

Room temperature powder X-ray diffraction (XRD) and (b) magnified view of (130) peak of the samples.

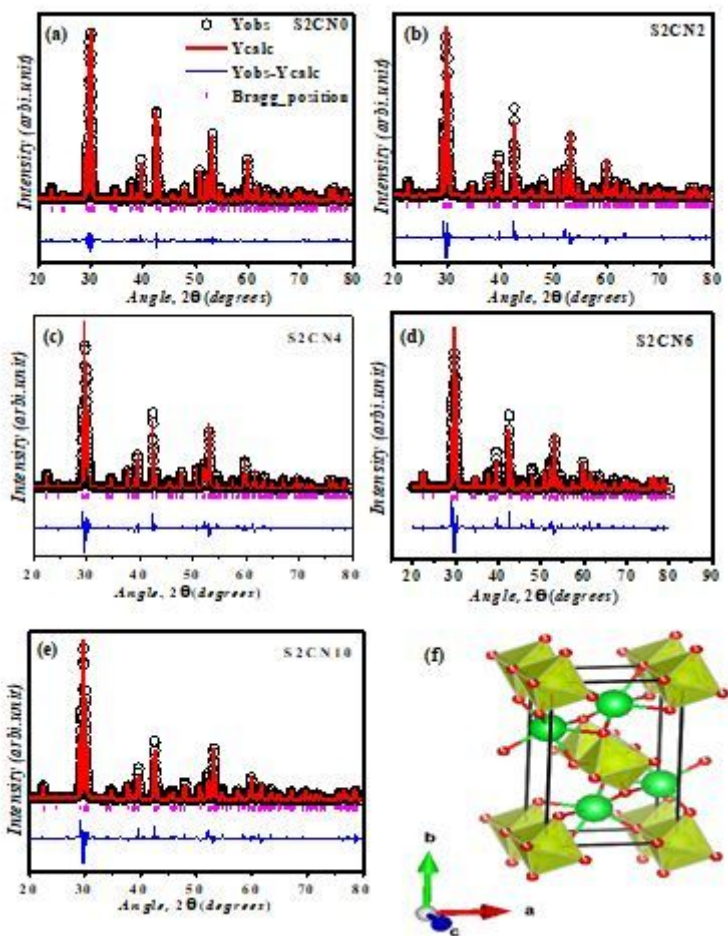


Figure 3

Rietveld refined XRD profile of the samples.

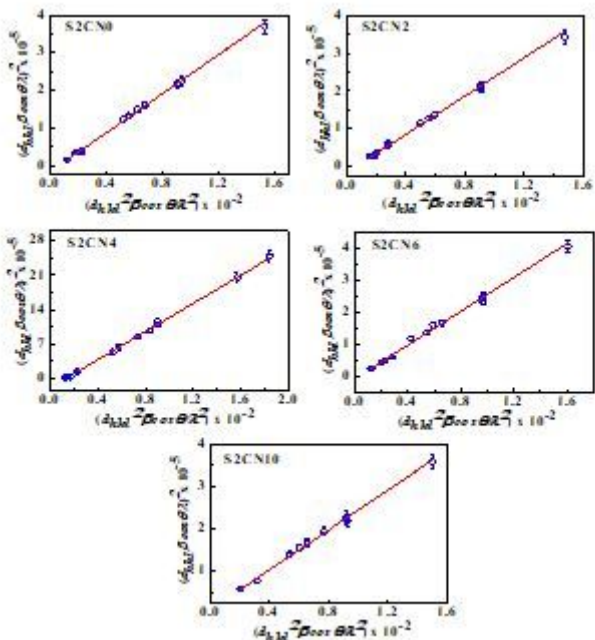


Figure 4

Size strain plots (SSP) for the determination of crystallite size and lattice strain of samples.

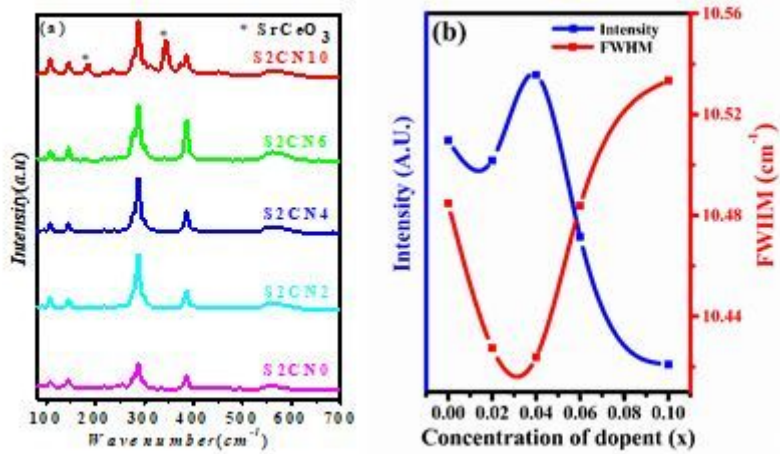


Figure 5

(a) Room temperature Raman spectra of all samples and (b) Variation of intensity and full width at half maxima for band 286 cm⁻¹ with concentration of dopant Na (x).

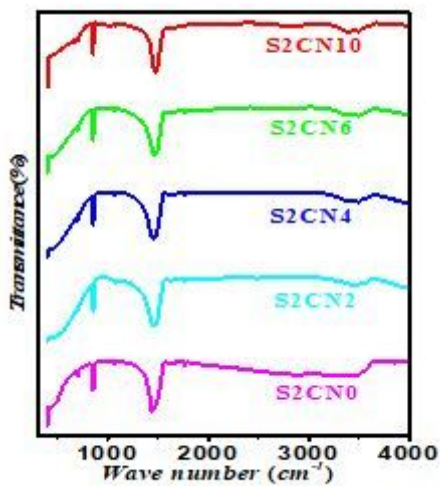


Figure 6

Room temperature Fourier Transform Infra-red (FTIR) spectra of the samples.

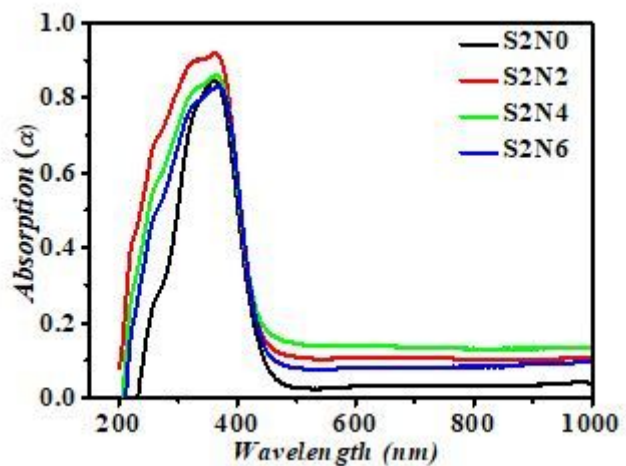


Figure 7

UV-visible absorption spectra of the samples.

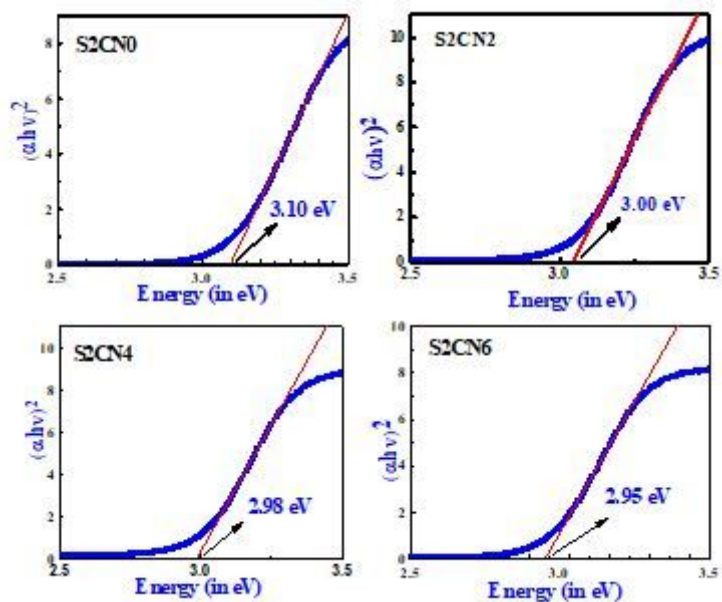


Figure 8

Tauc plots for the direct band transition.

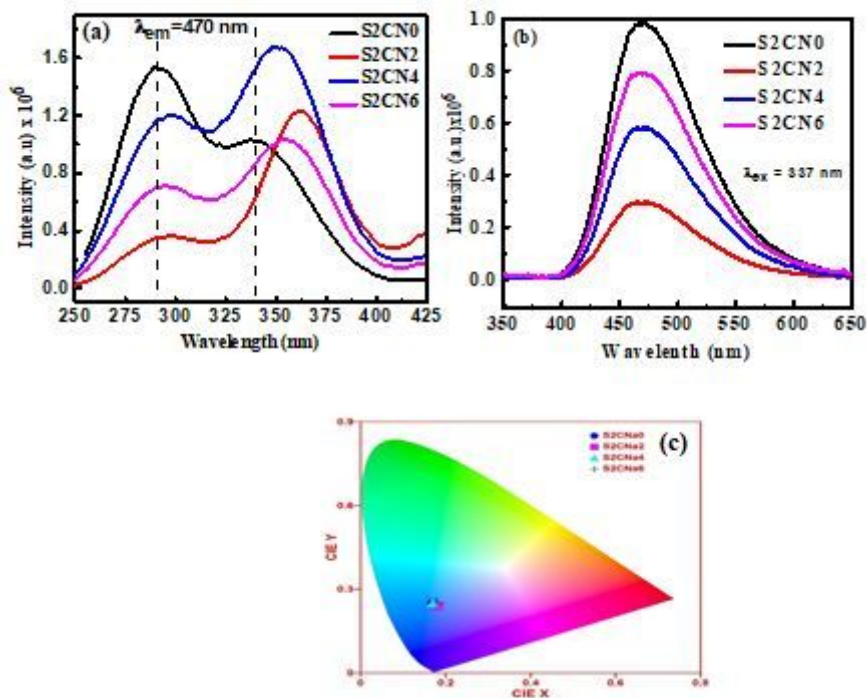


Figure 9

(a) Excitation spectra ($\lambda_{em} = 470 \text{ nm}$) (b) Emission spectra ($\lambda_{ex} = 337 \text{ nm}$) and (c) CIE co-ordinate diagram of prepared samples $\text{Sr}_2\text{Ce}_{1-x}\text{Na}_x\text{O}_{4-\delta}$ ($0 \leq x \leq 0.10$) calcined at 1100°C

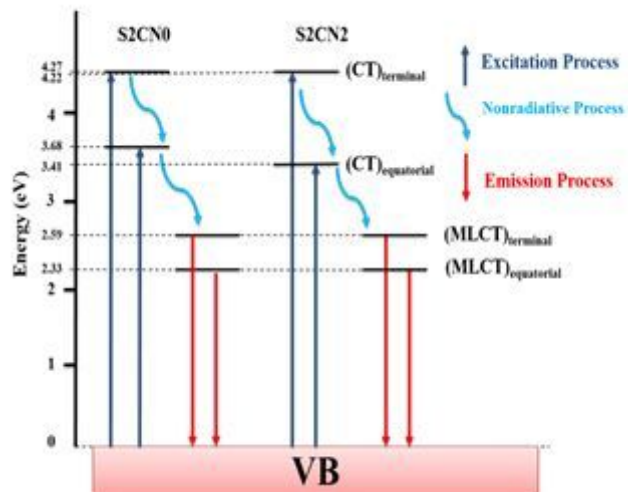


Figure 10

Schematic diagram of energy level for S2CN0 and S2CN2 samples.

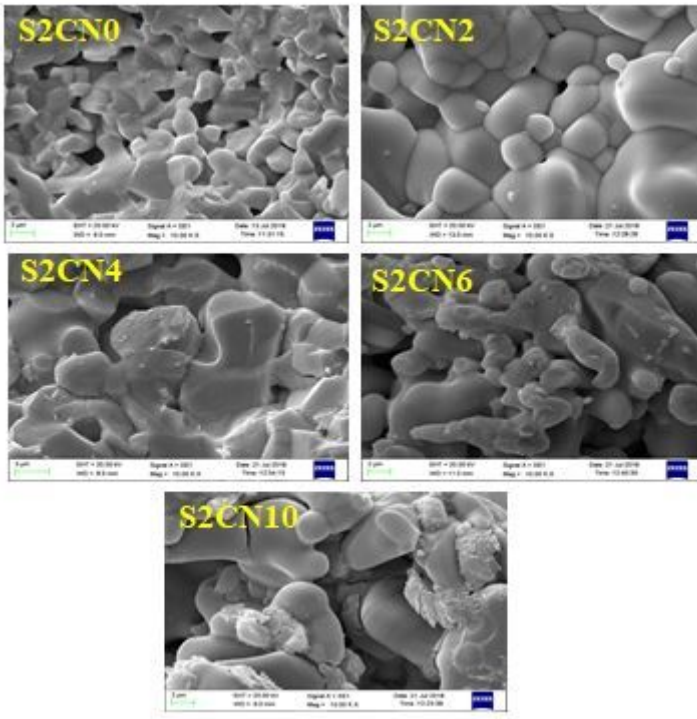


Figure 11

Scanning electron micrograph (SEM) of fractured surfaces of prepared samples.